fluids

MDPI

Article

Evaluating the Impact of Domain Boundaries on Hemodynamics in Intracranial Aneurysms within the Circle of Willis

Pablo Jeken-Rico [1], Aurèle Goetz [1], Philippe Meliga [1], Aurélien Larcher [1], Yigit Özpeynirci [2] and Elie Hachem [1,*]

[1] Mines Paris, Université PSL, Centre de Mise en Forme des Matériaux (CEMEF), UMR7635 CNRS, 06904 Sophia Antipolis, France; pablo.jeken_rico@minesparis.psl.eu (P.J.-R.)
[2] Institute of Neuroradiology, University Hospital LMU Munich, 81377 Munich, Germany; yigit.oezpeynirci@med.uni-muenchen.de
* Correspondence: elie.hachem@minesparis.psl.eu

Abstract: Hemodynamic simulations are increasingly used to study vascular diseases such as Intracranial Aneurysms (IA) and to further develop treatment options. However, due to limited data, certain aspects must rely on heuristics, especially at the simulation's distal ends. In the literature, Murray's Law is often used to model the outflow split based on vessel cross-section area; however, this poses challenges for the communicating arteries in the Circle of Willis (CoW). In this study, we contribute by assessing the impact of Murray's Law in patient-specific geometries featuring IA at the posterior communication. We simulate different domain extensions representing common modelling choices and establish Full CoW simulations as a baseline to evaluate the effect of these modelling assumptions on hemodynamic indicators, focusing on IA growth and rupture-related factors such as the Wall Shear Stress (WSS) and Oscillatory Shear Index (OSI). Our findings reveal qualitative alterations in hemodynamics when not modeling posterior communication. Comparisons between computing the anterior circulation and computing the whole Circle of Willis reveal that quantitative changes in WSS may reach up to 80%, highlighting the significance of modelling choices in assessing IA risks and treatment strategies.

Keywords: computational hemodynamics; intracranial aneurysms; Circle of Willis; wall shear stress; boundary conditions

Citation: Jeken-Rico, P.; Goetz, A.; Meliga, P.; Larcher, A.; Özpeynirci, Y.; Hachem, E. Evaluating the Impact of Domain Boundaries on Hemodynamics in Intracranial Aneurysms within the Circle of Willis. *Fluids* **2024**, *9*, 1. https://doi.org/10.3390/fluids9010001

Academic Editors: Fang-Bao Tian and D. Andrew S. Rees

Received: 21 October 2023
Revised: 23 November 2023
Accepted: 18 December 2023
Published: 21 December 2023

1. Introduction

Intracranial Aneurysms (IA) are estimated to affect about 3.2% of the adult population. While the annual risk of rupture is moderate at 2.2%, they impose a significant burden on patients, physicians, and the healthcare system [1,2]. To prevent ruptures, considerable effort is invested in early diagnosis, growth prediction, and treatment of IA. Advances in non-invasive imaging techniques such as Magnetic Resonance Angiography (MRA) have made regular preventive screenings increasingly feasible. Detecting IA at an early stage provides neuroradiologists with the opportunity to weigh treatment options or continue monitoring the aneurysm's evolution. In this decision process, physicians rely on geometrical and topological characterization of the IA along with other patient records. While scoring methods based on statistics such as the PHASES score may contribute to the decision-making process, they have been shown to be weak overall predictors [3].

Instead of relying solely on statistics, Computational Fluid Mechanics (CFD) has been proposed as a promising complementary tool. The goal is to simulate the hemodynamics of IA and extract risk indicators in order to assess the severity of the case and potentially predict a rupture site. Despite substantial progress in this field [4–6], a latent dissent exists in the research community, highlighted during numerous CFD challenges. It has been confirmed that due to their various modeling strategies the participating teams obtained dissimilar results that, in certain cases, could point towards different interpretations [7–10]. For a consolidated use of CFD in IA research, it is imperative to address open modelling questions in advance [11].

Outflow Boundary Conditions (BCs) represent one recurring source of uncertainty in vascular fluid dynamics. Reliable measurements are challenging to obtain, and as such are rarely employed [11]. Instead, the Principle of Minimum Work can be used to prescribe the flow split among the distal ends of the simulated network based on the relationship of their cross-sectional areas [12]. This heuristic, arising from the pursuit of minimizing the energy spent on the transport and storage of blood, has been confirmed through ex vivo analysis by analyzing the regularity of arterial branching patterns [13]. The Law of Minimum Work, known as Murray's law, is not only more realistic than plain stress-free outflows [14,15], it offers the advantage that it solely depends on the geometrical features of the network. This is advantageous because it makes boundary conditions reproducible across varying modeling assumptions such as rheology laws, solver schemes, and boundary extrusions.

Nevertheless, Murray's law has an unstudied implication when applied to the communicating arteries in the Circle of Willis (CoW), a loop of arteries found at the base of the brain (see Figure 1). From an anatomical point of view, these vessels serve the purpose of linking the anterior and posterior circulations, thereby providing alternative pathways for the blood in case of ischemia [16]. Frequently, the PCom carries a lesser net flow from the ICA to the PCA, although different CoW configurations may perturb this rule [17–19]. The majority of CFD studies that examine IA at the carotid arteries only consider one part of the anterior circulation, either defining the PCom as a regular system outlet [14,20] or neglecting it [21,22]. These two strategies pose two extreme cases, and inevitably raise the question of whether or not they lead to physiological conditions.

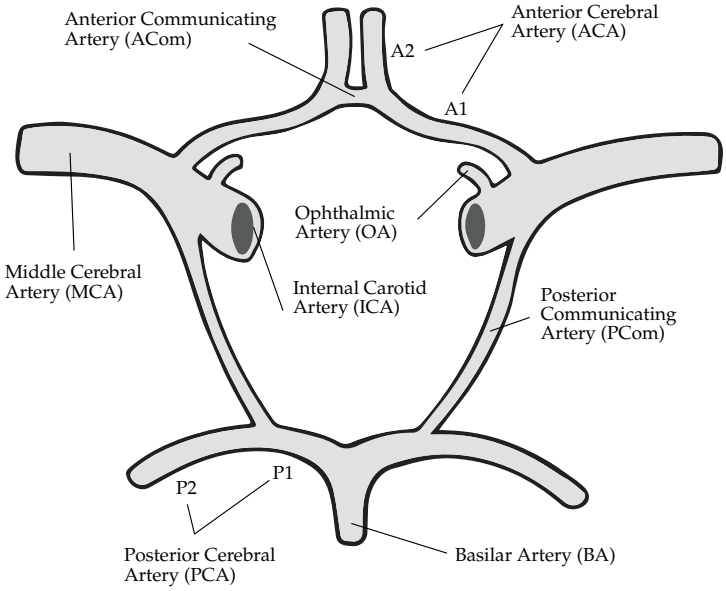

Figure 1. Schematic view of the complete CoW and the ophthalmic arteries.

The uncertainty surrounding the simulation domain of IA and the uncertainty in treating the PCom artery in CFD, as per the existing literature, underscores the motivation for this study. Our aim is to evaluate changes in intra-aneurysmal hemodynamics in ICA-PCom bifurcation aneurysms by varying the extent of the simulated vasculature. These extensions are selected based on common observations from the IA literature, and are compared with full CoW simulations. The primary focus of the comparison lies in intra-aneurysmal flow patterns and the exposure of the lumen to shear stresses.

2. Materials and Methods

2.1. Medical Imaging and Segmentation

Angiographic images were obtained using time-of-flight angiography on 1.5 T and 3 T MRI scanners with isotropic imaging and 0.6 mm slice thickness. The lumen was segmented using 3DSlicer (https://www.slicer.org/, accessed on 5 May 2023) under the supervision of neuroradiologists of the cooperating medical institution. Patient A has a complete CoW

with one aneurysm of diameter 7.5 mm at the left ICA-PCom bifurcation. Patient B has a bilateral P1 hypoplasia, and as such is missing a connection of the basilar artery with both anterior circulations. The PComs are defined in this case as fetal, as their size is larger than usual and they are in fact the main supplier of blood to the PCA [23]. The aneurysm of the latter is located on the right side ($d = 5$ mm) and features a pronounced lateral daughter sack. The complex geometry of this formation was later confirmed through image recordings during the operation procedure. Lastly, patient C has an incomplete CoW due to an absent right PCom. In this case, two IAs can be found, one at the left ICA-PCom bifurcation and one at the right MCA bifurcation. The former, which was the only one considered during analysis, is classified as bilobular due to the presence of two rounded sacks.

2.2. Spatial Discretization

For each of the segmented geometries, three extensions of ascending complexity (see Figure 2) were generated to assess the implications of Murray's law on simulated hemodynamics. Geometries with the keyword Simplified are constrained to the main supplying artery that leads to the IA. Communicating arteries and A2 segments (see Figure 1) are neglected in this case. Middle extends the prior Simplified complexity by adding the PCom. Finally, the keyword Full denotes the full CoW. To minimize perturbations caused by inlet and outlet models, extrusions were made along these boundary patches [11,21]. Circular profiles were adapted by a least-square fit to the irregular vessel cross-sections and extended along the mean vessel direction using transfinite interpolations. This procedure additionally simplifies the imposition of circular inflow profiles and facilitates geometrical information required for the outflow boundary conditions.

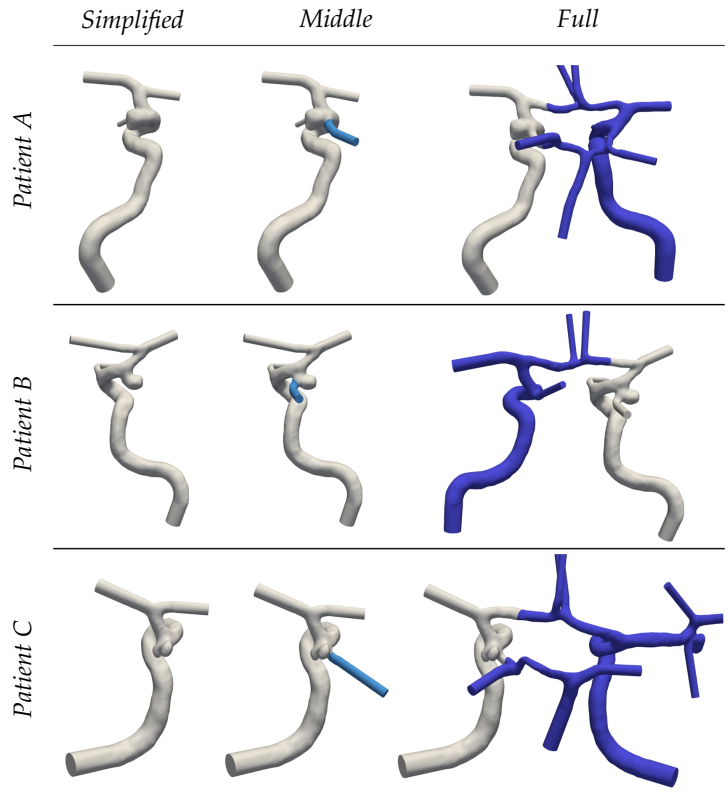

Figure 2. Overview of cases A–C (**top** to **bottom**) in the different extensions Simplified–Full (**left** to **right**). Simplified—Neglection of the adjacent PCom. Middle—Simulation of ICA and proximal vessels. Full—Full computation of the CoW.

The open 2D surface meshes were parametrized using conformal maps, remeshed, and extruded inwards to generate a set of tetrahaedral boundary layers (growth factor 1.2) [24]. These boundary layers serve two crucial purposes in our fluid simulations of arteries. First,

the incorporation of boundary layers is essential for a more accurate resolution at the wall regions. Second, maintaining consistency in the structure at the boundaries permits comparison between different cases without disturbances from mesh-induced boundary effects. The layer thickness was determined based on the dimensionless wall distance of $y^+ = 1$, an overestimated Reynolds number of $Re = 1000$ and the averaged diameter of the ICAs. As proposed in [4], we fixed the mesh size $h = 0.2$ mm based on a preliminary mesh convergence, which was progressively refined to $h = 0.1$ mm at the aneurysm periphery (see Figure 3) utilizing gmsh (https://gmsh.info/, accessed on 30 May 2023).

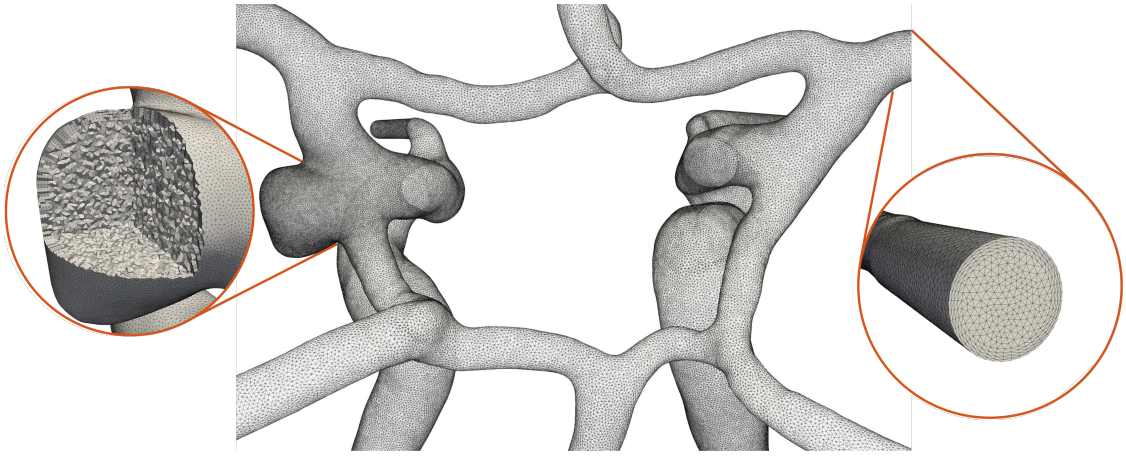

Figure 3. Visualization of the CoW of patient A with highlighted mesh features (orange circles) showing the linear isotropic refinement (**left**) and structured tetrahaedral boundary layers (**right**).

2.3. Hemodynamics Simulations

2.3.1. Navier–Stokes

Simulations were carried out by numerically solving the transient incompressible Navier–Stokes equations using an in-house Finite Element (FE) solver. The discrete system is set up by linear elements for both pressure and velocity, and is consequently stabilized by a residual-based Variational Multiscale-type method [25,26]. The weak formulation (see Equations (1) and (2)) is enriched with the residuals of continuity $\mathcal{R}_C$ and residuals of momentum $\mathcal{R}_M$. For details on the stabilization parameters (τ_C and τ_M), see [25] and references therein. Time integration was carried out with a second-order semi-implicit backwards scheme, which has been shown to provide a good balance between memory and consistency [27,28].

$$\int_\Omega \underbrace{\rho(\partial_t \vec{u}_h + (\vec{u}_h \cdot \nabla)\vec{u}_h) \cdot \vec{w} + \sigma : \nabla \vec{w}}_{\text{Galerkin terms}} \, d\Omega + \sum_{\Omega_e \in \Omega} \int_{\Omega_e} \underbrace{\tau_M \rho(\vec{u}_h \cdot \nabla)\vec{w} \cdot \mathcal{R}_M}_{\text{Upwind stabilization}} \, d\Omega$$
$$+ \sum_{\Omega_e \in \Omega} \int_{\Omega_e} \underbrace{\tau_C \mathcal{R}_C \rho \nabla \cdot \vec{w}}_{\text{Grad-div stabilization}} \, d\Omega = \int_{\Gamma_h} \underbrace{\vec{w} \cdot \sigma \cdot \vec{n}}_{\text{Boundary stress}} \, d\Gamma, \quad \forall \vec{w} \in H^1 \tag{1}$$

$$\sum_{\Omega_e \in \Omega} \int_{\Omega_e} \underbrace{\tau_M \nabla q \cdot \mathcal{R}_M}_{\text{Pressure stabilization}} \, d\Omega + \int_\Omega \underbrace{q \nabla \cdot \vec{u}_h}_{\text{Galerkin term}} \, d\Omega = 0, \quad \forall q \in H^1 \tag{2}$$

As mentioned previously, several benchmark validations with both space and time convergences analyses were made in [25,27], and more recently in the context of IA in [29]. The obtained parameters yielded stable simulations and matched the proposed resolutions in the IA and hemodynamics literature [4,22,30]. For completeness, we added the effects of different timesteps and mesh resolutions (see Figures 4 and 5) on a representative test case, patient B, allowing us to finally fix the time step to 1 ms and the mesh size graduation between $h = 0.2$ mm and $h = 0.1$ mm at the aneurysm periphery for for all our simulations.

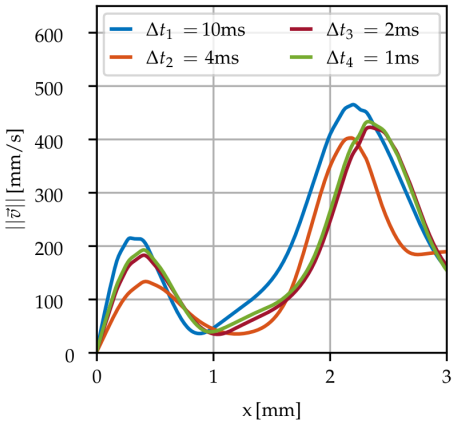

Figure 4. Velocity profile over aneurysm B for different time resolutions using the described mesh.

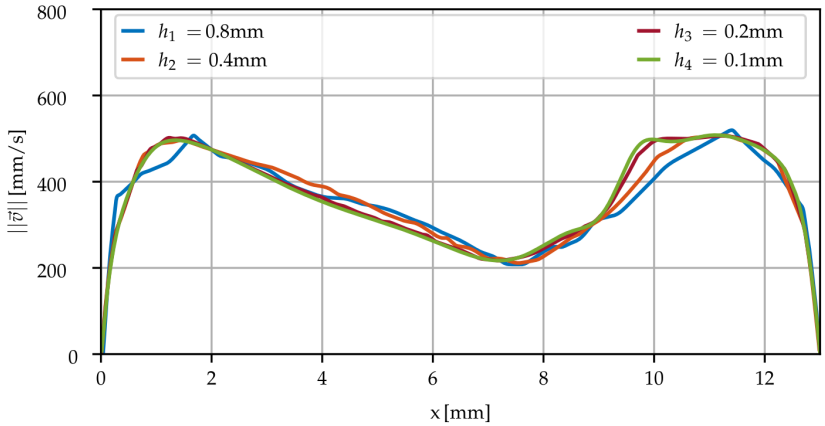

Figure 5. Velocity profile plotted over the C6-C7 ICA sections (Patient B) for different mesh sizes.

2.3.2. Rheology

The shear-thinning rheology was modelled through the Carreau model describing its behaviour [11,31,32], as provided in Equation (3). The constants $\rho = 1056\,\mathrm{kg/m^3}$, $\mu_0 = 0.0456$ Pa·s, $\mu_\infty = 0.0032$ Pa·s, $\lambda = 10.03$ s, and $n = 0.344$ and shear rate $\dot{\gamma}$ were employed [33].

$$\mu(\dot{\gamma}) = \mu_\infty + (\mu_0 - \mu_\infty)\left(1 + (\lambda\dot{\gamma})^2\right)^{(n-1)/2} \tag{3}$$

2.3.3. Boundary Conditions

Inflow conditions were described with the help of a generalized volumetric flow curve which was scaled and split among the supplying arteries (see Figure 6). More precisely, in case A each ICA contributes 44% of the total volumetric flow, while the BA carries only 12% due to its small size [34]. Cases B and C follow a split of 40%–20% between each ICA and the BA. The flow rate Q was imposed via parabolic velocity profiles at the base of the arterial system. The walls were considered fully rigid, and as such were set through no-slip conditions.

The outflow of the system followed Murray's Law, guiding the flow distribution based on the cubed outlet radius, as expressed in Equation (4) [14,15]. The exponent three (n = 3) aligns with Poiseuille flow assumptions on the long-term cost of blood transport in brain arteries [12]. This exponent was chosen for consistency with the linear relationship $P = QR$ used to impose the desired flow rates. The rule is derived from fully established Poiseuille flow principles [35], and is commonly used in brain arteries [28,36]. The resistances R were

adjusted iteratively for each outlet, ensuring a systematic application of Murray's Law across the system.

$$Q_{out,i}(t) = Q_{in}(t)\frac{r_i^3}{\sum_j r_j^3} \tag{4}$$

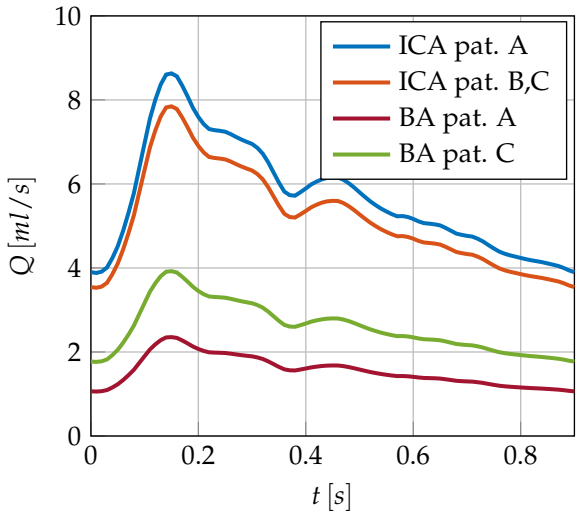

Figure 6. Volumetric inflow of patients A–C.

2.3.4. Computation Details

For the solution, the fully coupled system of pressure and velocity was solved in parallel using the ILU(4) block preconditioned Stabilized Bi-Conjugate Gradient method. The simulations were carried out on dual processors (32-Core AMD EPYC 64-bit Processor 7502, Advanced Micro Devices, Santa Clara, CA, USA) with a 2.5 GHz base clock rate and a HDR 100 interconnection. The computing times of each cardiac cycle can be extracted from Table 1. The number of elements, likewise provided in Table 1, was notably higher for case A due to its larger volume and aneurysm sack.

Table 1. Element count in millions of elements and computation time per cardiac cycle of different meshes.

	Patient	Simplified	Middle	Full
A	n_{elem}	3.4	3.8	7.1
	T_{comp}	9:20 h	10:12 h	22:10 h
B	n_{elem}	2.0	2.1	3.6
	T_{comp}	4:41 h	5:19 h	8:23 h
C	n_{elem}	1.6	1.7	4.7
	T_{comp}	5:07 h	5:46 h	8:30 h

2.4. Hemodynamic Descriptors

The influence of different domain extensions was assessed through key hemodynamic indicators, including Wall Shear Stress(WSS), Oscillatory Shear Index (OSI), and velocity profiles. As a primal variable, velocity is inherently linked to any alterations in system dynamics, and as such was considered for initial assessments. WSS and OSI belong to a set of indicators related to vascular remodeling, and are recognized as risk factors in aneurysm formation [37–39]. According to Meng et al. [40], destructive remodeling phenomena of arterial walls can be categorized into mural cell-mediated events caused by abnormally high WSS and inflammatory remodeling induced by low WSS and high OSI. However, despite the identification of general trends in the literature [41], a consensus on threshold values for WSS and OSI in brain arteries remains elusive [42]. Recent advancements in hemodynamic research have introduced WSS-derived quantities such as the WSS gradient topology [43]

and the relative residence time (see [44] and therein). These novel indicators provide insights into the pulsatility and topological structure of WSS distributions. Recognizing the critical role of WSS in these advancements, our work primarily focuses on its accurate computation. These quantities were calculated from the velocity fields through the stress tensor σ, as illustrated in Equations (5) and (6), respectively.

$$\vec{\tau}_{wss} = \vec{n} \times (\sigma \cdot \vec{n}) \times \vec{n} \tag{5}$$

$$\mathrm{OSI} = \frac{1}{2}\left(1 - \frac{\left\|\int_0^T \vec{\tau}_{wss}\, dt\right\|}{\int_0^T \|\vec{\tau}_{wss}\|\, dt}\right) \tag{6}$$

3. Results

3.1. Simulations

The overall flow distribution can be visually followed from the velocity magnitudes shown in Figure 7. Patient A stands out due to slower flow velocities despite similar tributary flows, which is a direct consequence of having larger vessels overall compared to B and C. The plot highlights regions of high flow speeds, for instance in the terminal ICA bifurcation. The highly inertia-driven flow turns mostly into the MCAs, which due to both their size and the Murray exponent (n = 3) carry the largest outflow. When present, the BA supplies the posterior circulation of the brain without directly irrigating the anterior circulation. Therefore, the flux traversing the PCom is strictly unidirectional, carrying blood away from the ICA towards the PCA in accordance with the commonly observed flow direction [18,45]. According to our models, Patients B and C feed the distal PCA mostly (Patient C) or exclusively (Patient B) through the PCom due to their small or fetal P1 segments.

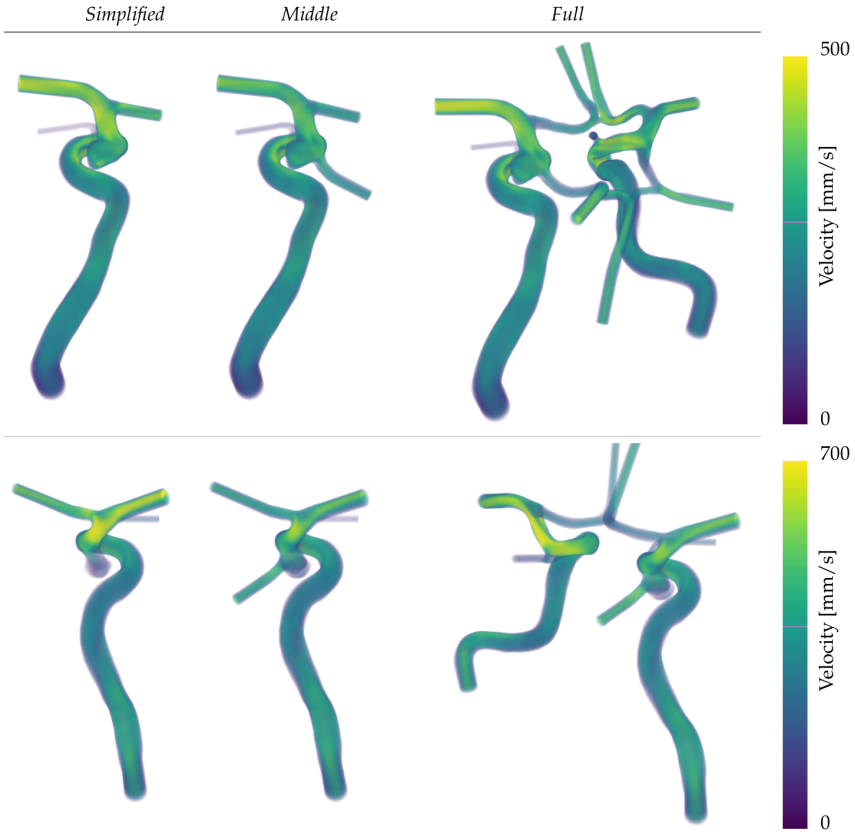

Figure 7. *Cont.*

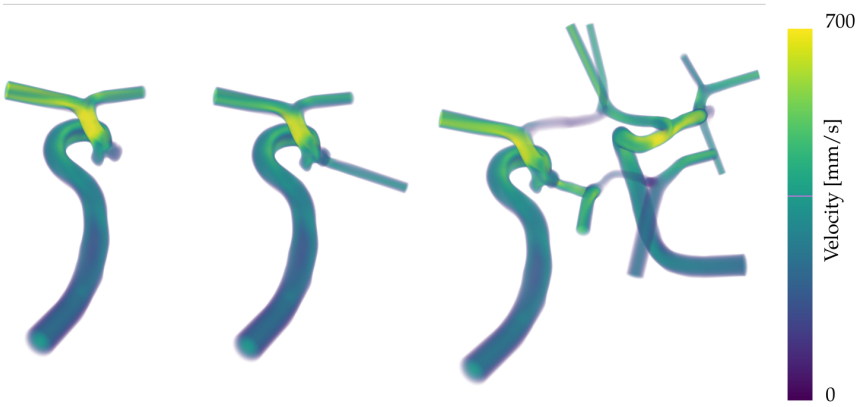

Figure 7. Maximum velocity projection of patients A–C (**top** to **bottom**) for all complexity levels Simplified–Full (**left** to **right**) at diastole.

The detailed presentation of the average blood transported through each vessel is provided in Table 2. Notably, in the Full configuration, the flow through the A2 segment of the ACA is consistently smaller, exhibiting a deviation of up to 5 percentage points compared to the Middle and Simplified configurations. The Middle configuration is characterized by guiding flow away from the MCA towards the A1 segment of the ACA, representing a distinct pattern in the distribution of the blood flow. These observations are relevant for the later discussion of the biases of Murray's law. Additionally, the volumetric flow was recorded at the vessels close to the aneurysms. Figure 8 shows this quantity normalized with respect to the maximum mean flow of the three extensions. It can be seen that in the Simplified simulations the flow that would leave through the PCom is distributed among the other outlets, causing their flow rates to be consistently higher. While Middle is distinguished from Full through lower outflows through the MCA and larger ones through the ACA, it exhibits no general trend on the PCom.

For verification purposes, the goodness of the boundary condition model is shown, for which the resistances R_i have been fitted in an iterative process to minimize the L_1 error between the targeted flow and the achieved one. In Figure 9, the volumetric flow of the left hemisphere's outlets (aneurysm A) are shown together with the targeted curves as a representative example of the fitting performance. The linear law enables the mass flow to be controlled through pressure BCs within a relative error of 5% per cardiac cycle despite non-Newtonian and transient flows. The largest relative deviations are observed at small vessels during peak systolic and peak diastolic times, for instance, the OA (green curves) in Figure 9.

Table 2. Outflow per cardiac cycle with respect to the in total inflow of each patient. In the Full configuration of case C, the flow in the right MCA is a consequence of imposing Murray's law on the vessels of the M1–M2 bifurcation. The massflow for the Middle and Simplified configurations is taken at the A1 ACA segment due to the inherent cut of the domain.

Case	Complexity	MCA		PCA		ACA		OA	
		Left	**Right**	**Left**	**Right**	**Left**	**Right**	**Left**	**Right**
A	Full	28.8%	25.7%	14.0%	7.7%	7.2%	9.3%	3.1%	4.2%
	Middle	21.8%	-	10.6%	-	9.2%	-	2.4%	-
	Simplified	28.8%	-	-	-	12.1%	-	3.1%	-
B	Full	29.3%	21.6%	4.9%	9.6%	4.3%	7.0%	-	3.1%
	Middle	-	20.9%	-	9.3%	-	6.8%	-	3.1%
	Simplified	-	27.2%	-	-	-	8.8%	-	4.0%
C	Full	27.1%	35.9%	12.0%	12.4%	4.0%	8.5%	-	-
	Middle	22.1%	-	7.5%	-	10.3%	-	-	-
	Simplified	27.3%	-	-	-	12.7%	-	-	-

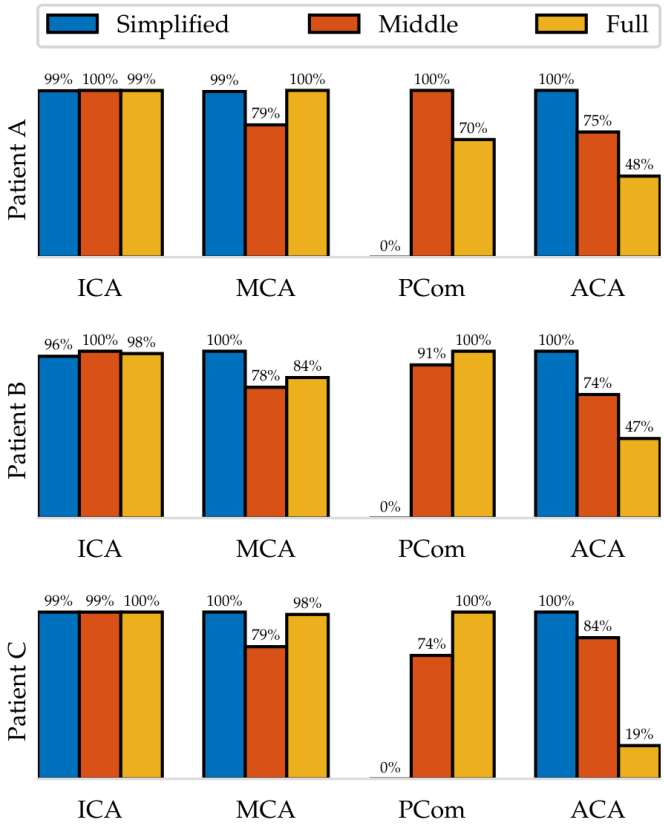

Figure 8. Mean volumetric flow per cardiac cycle in the IA proximity. The percentage values describe how much flow passes through the indicated vessel with respect to the other configurations. The cuts of the MCA and ACA are set at the M1 and A1 segments, respectively.

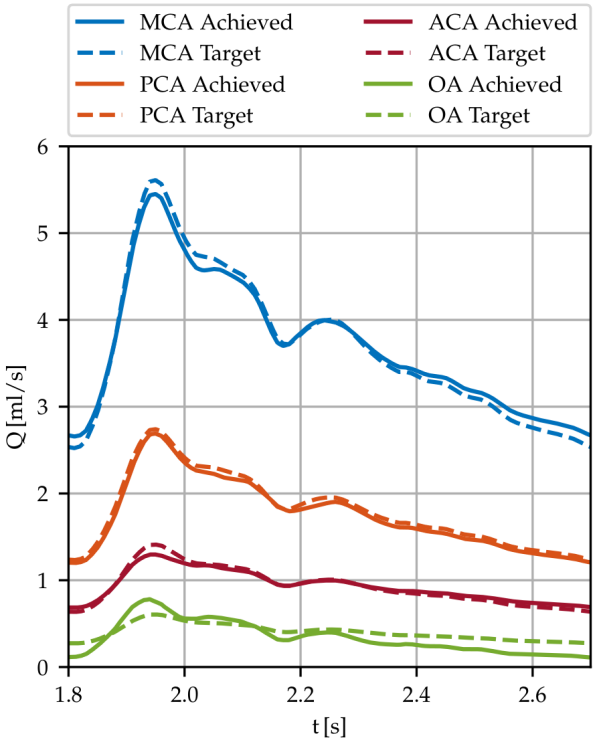

Figure 9. Volumetric flow through the left ICA outlets of patient A, comparing the values of the targeted flow (dashed lines) as dictated by Murray's Law (see Equation (4)) with those obtained using the linear pressure relationship $P = QR$ after fitting the resistances.

3.2. Intra-Aneurysmal Dynamics

The flow structures in the domes are visualized in Figure 10 for each patient (rows) and configuration (columns). The aneurysms are cut with a plane at the neck, and velocity streamlines of the intra-aneurysmal flow are inscribed lightly to indicate the structure of the present vortices at peak diastolic time. For the inertial flow of aneurysm A (first row), all three configurations show a large centred vortex traversing the dome that can be regarded as consistent across the three sizes. On the contrary, Patients B and C in the second and third rows of Figure 10 display clear discrepancies. Starting with aneurysm B (second row), it is apparent that in the simple configuration the main inflow enters the dome focused as a small jet, then later decays into a stable weaker recirculation. For the Middle and Full extensions of the same case, the inflow hits the neck of the daughter sack, splitting its momentum among two vortices that traverse the main lobe and the daughter sack, respectively. In the Full simulation of B (second row, third column), the daughter sack's recirculation is located farther up inside the dome, leading to larger in-plane velocities. Lastly, Patient C (the third row of Figure 10) presents the largest disparities on both the quantitative and qualitative levels. One of the most noticeable differences in Figure 10 is the inverted circulation of the right aneurysm dome with respect to the other two extensions in the *Full* simulation. At the same time, the average velocity of the impinging jet exceeds those in the other cases by 31% and 19%, respectively.

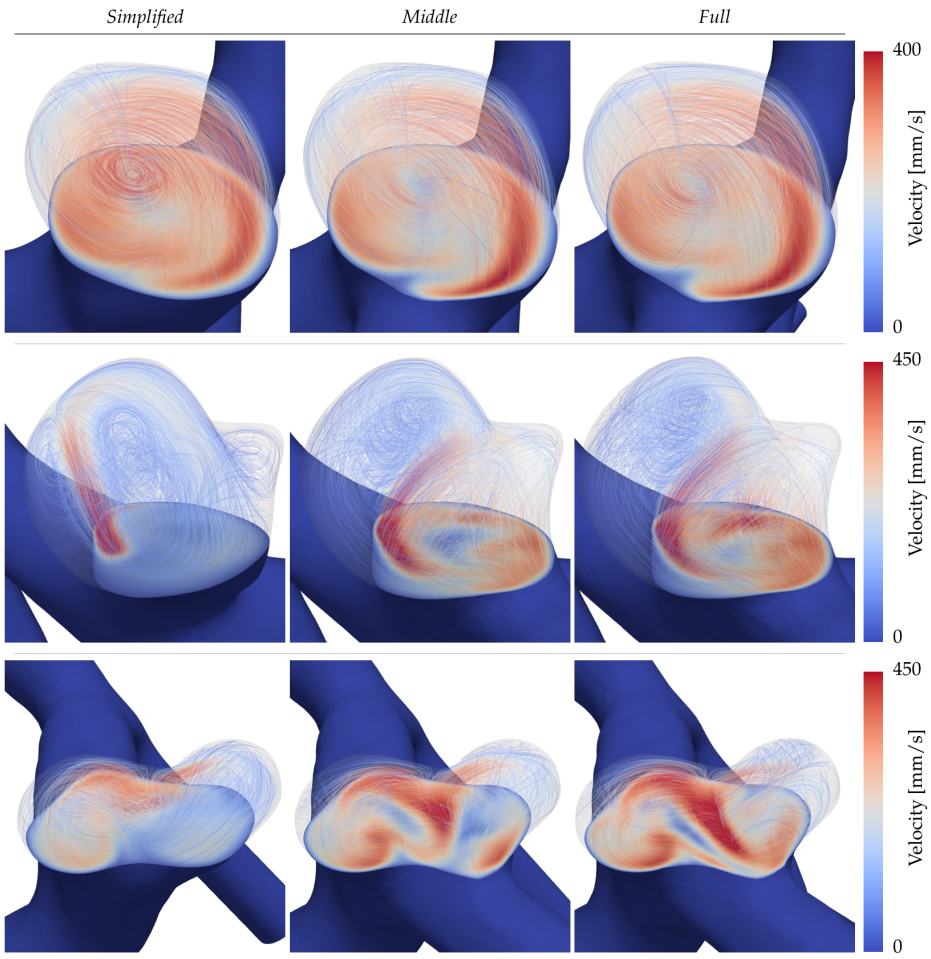

Figure 10. Cross-section cuts at the IA neck of Patients A–C (**top** to **bottom**) with the inscribed velocity magnitudes at diastole. The velocity streamlines are superposed with the aneurysm necks to highlight the structure of the flow.

3.3. Wall Shear Stress

The WSS magnitudes for peak diastole and systole are shown in Figure 11a,b, respectively. Patient A (first row) is characterized by a stable and qualitatively similar WSS pattern across all extensions. Here, only the Simplified case demonstrates smaller patches of higher shearing that are not present in the Middle and Full systems. Patients B and C instead exhibit persistently altered WSS patterns for all of the domain extensions. Setting the Simplified system aside, it is possible to observe shifts in patterns between the Middle and Full extensions in the second and third columns, respectively. Most notable here is the daughter sack in patient B's aneurysm (second row of Figure 11). During diastole, the WSS is relatable between the Middle and Full systems. On the contrary, at systole the shearing increases for the Middle system while remaining low for the Full system, leading to two distinct characterizations. Following the Full system, the daughter sack could be identified as a risk factor due to low WSS exposure, whereas the Middle simulation would not. Daughter sacks play an important role here, as their appearance is linked to an augmented risk of rupture. The last patient case in the bottom row of Figure 11a,b, again shows an inconsistent WSS among the different extensions, which is especially aggravated at the dent separating the two sacks.

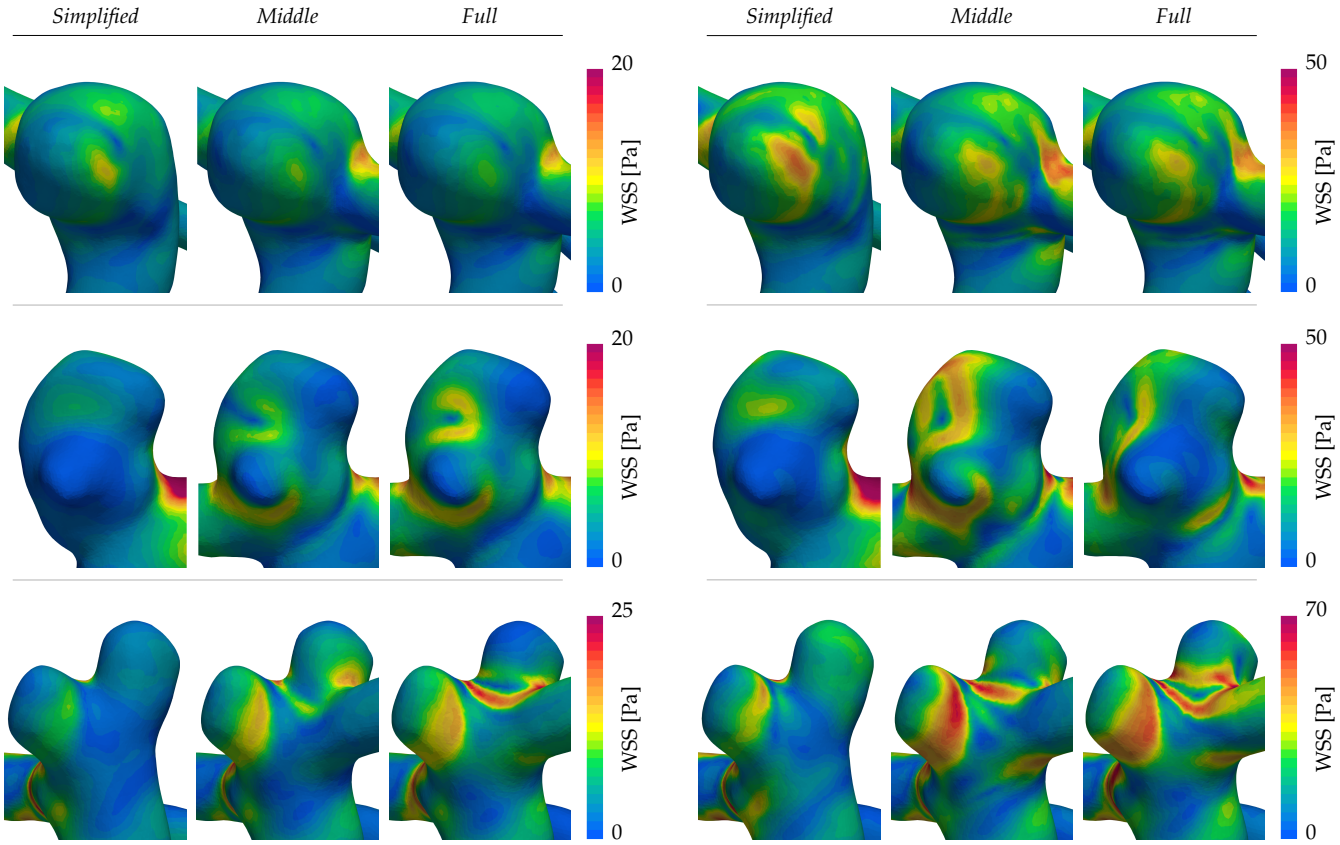

(**a**) Diastolic WSS (**b**) Systolic WSS

Figure 11. WSS distributions on aneurysms A–C (**top** to **bottom**) for the different complexity levels at diastole (**a**) and peak systole (**b**).

3.4. Oscillatory Shearing

Following the same structure as in Figure 11a,b, the OSI is displayed in Figure 12. The observed stable WSS profile of aneurysm A inevitably leads to nearly absent oscillatory shearing with only small localized peaks (see the first row in Figure 12). Large dissent of the OSI distributions is again found in patients B and C (the second and third rows of Figure 12), which is especially apparent in the distal lobe of Patient C. There, in contrast to the other cases, high overall values are found on the visible face in the Full CoW simulation.

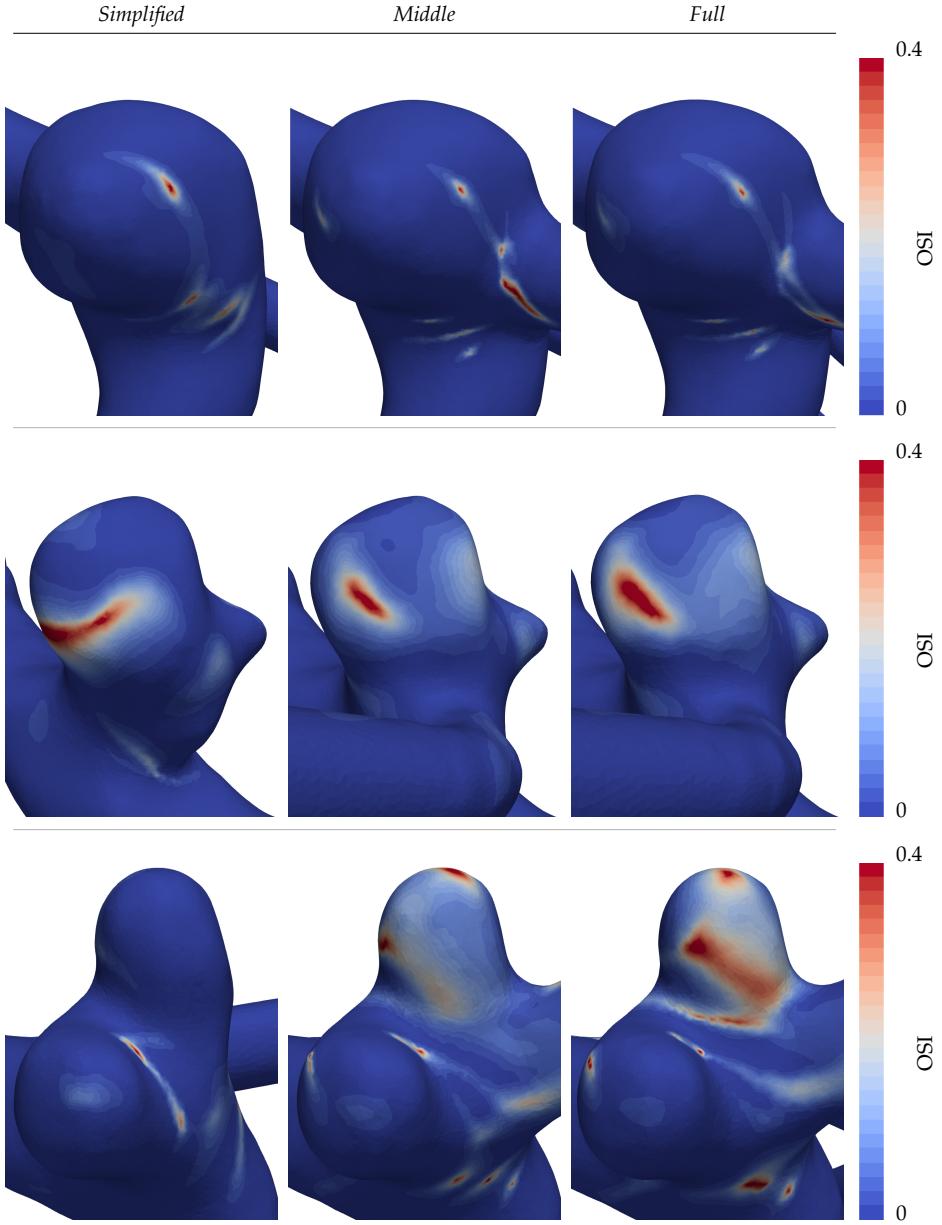

Figure 12. OSI distributions for cases A–C (**top** to **bottom**) under different geometry extensions.

4. Discussion

The results show a satisfactory application of resistive boundary conditions to the simulation of hemodynamics, providing accuracies above 95% with respect to the targeted flows of Murray's law. The resulting flow in the CoW resembles the values from the literature [46], though with a tendency to overestimate the flow through the MCAs. Using an exponent of (n = 2) in Murray's law (see Equation (4)) reduces the discrepancy for the flow in the MCA, though at the cost of overestimating the flows in smaller vessels such as the OA. Detailed measurements of brain arterial trees [13] suggests that Murray's law is best fit by exponents that grow from 2 in the proximal sections towards 3 in the more distal sections. While this factor is important to consider in general, we opted for a consistent modelling of the distal systems based on the Poiseulle flow. For a more detailed analysis of this matter, refer to [15,20], which studied the different exponents, area estimations, and bifurcation rules in relationship with Murray's law.

The changes in the flow through the ACA between the different computational domain extensions are a direct consequence of Murray's law being applied to vessels of varying diameter. In all cases, the proximal ACA (A1) has a larger radius than its post-

communicating segment (A2), leading to different flow rates according to Equation (4). However, this apparent inconsistency is caused by perforator vessels around the ACom, such as the Recurrent Artery of Heubner, which due to their small size cannot be properly simulated. Experimental studies [46] support the observed decrease in flow rates. In our cases, applying Murray's law shows better agreement with the aforementioned study in both ACA and MCA flow rates when setting the domain boundary in the A1 segment.

Further analysis of the hemodynamics in the IA shows differences that exceed expectations, comparable to those seen in simulation challenges [7,8,10]. The Simplified strategy lacks physical reasoning, as all of the patient geometries in this study exhibit PCom arteries. Simulations confirm that neglecting these arteries significantly alters the intrasaccular hemodynamics, confirming the initial intuition. Without further exploration of this strategy, we conclude that it is unsuitable for the presented vasculatures.

The Middle extension, commonly found in the literature, presents more similarities with the Full CoW simulations. However, moderate changes in hemodynamics sometimes result in magnified alterations in WSS. These differences may lead to varied correlations between the flow dynamics and aneurysm evolution [28]. Causes for these observations include changed boundary flow rates on one side and a lack of interactions with the opposing hemisphere and posterior circulation on the other.

The additional blood suppliers in the case of the Full simulations, such as the neighbouring ICA and the BA, are participants in causing blood to traverse communicating vessels into other circulation segments. Although most of the interhemispheric flow was observed at the ACom, making it distal to the aneurysm fundus, the importance of the inflow streams' influence cannot be generally disregarded [21]. Due to a lack of measurement data, we imposed equal flow rates for the ICAs, aligning with a popular choice demonstrated in [7]. As stated before, this is irrefutably one of the biases taken into consideration that could be lifted by measurements in follow-up work. The second factor causing altered results between the Full CoW and Middle simulations, as stated earlier, is the interaction between the anterior and posterior circulations. By not imposing a midway boundary in a posterior communicating artery, more slack exists for the flow to unravel its natural characteristics, thereby providing a more physiological hemodynamic profile. Examples of this, among others, are pressure drops at posterior arterial junctions and bifurcations that effectively alter upstream pressure distributions, and are of notable relevance [14,47].

The flow in these communicating vessels holds significant medical importance, considering that 60–70% of all IAs are located on the Circle of Willis, which itself constitutes 85% of all IAs [48]. These vessels are both abundant and intricate, often presenting challenges in treatment due to their small size and contributing substantially to the incidence of ruptures [49]. While the role of CFD in diagnosing and analyzing IA growth and remodeling processes remains uncertain, it is crucial to acknowledge that modeling choices significantly impact the hemodynamics of communicating vessels [50]. Moreover, statistical evidence indicates that the absence or hypoplasia of certain communicating segments is associated with a higher likelihood of developing IAs [51,52]. As such, it becomes imperative to continually evaluate and refine CFD models in order to capture the hemodynamics of the CoW more effectively. This ongoing consideration is essential for advancing research and addressing the multitude of unanswered questions surrounding intracranial aneurysms.

5. Conclusions

In this study, we have conducted a detailed analysis of how different domain extensions and complexity levels affect hemodynamics in the brain's Circle of Willis. Using patient-specific geometries and computational fluid dynamics, we simulated three models of increasing complexity inspired by common literature findings for each patient. All of these simulations considered non-Newtonian pulsatile fluid flow, and outflow splits were determined using Murray's law.

The obtained results showed notable variations in flow patterns throughout the arterial network, particularly in two of the three cases. This highlights the importance of carefully analyzing topology in order to avoid modelling errors and conflicting results.

We conclude that studying the patient-specific Circle of Willis anatomy or utilizing measurement data is important for analysis of hemodynamic risk indicators in order to ensure physiological hemodynamics. To balance computational demands and accuracy, we suggest a two-step approach: a coarse large-scale simulation of the CoW to provide boundary conditions, and a highly resolved local simulation focused on the region of interest, ensuring both reliability and high-fidelity hemodynamics. This approach can be applied to other vascular pathologies as well.

This study deals with the modelling challenge in IA research, which, if addressed comprehensively, could reduce discrepancies in computational fluid dynamics results, enhancing our understanding of IAs and their treatment principles.

Author Contributions: Conceptualization, P.J.-R. and A.G.; methodology, P.J.-R.; software, A.L.; validation, P.J.-R., P.M. and A.G.; formal analysis, P.J.-R.; investigation, P.J.-R.; resources, Y.Ö.; data curation, Y.Ö.; writing—original draft preparation, P.J.-R.; writing—review and editing, A.G. and P.M.; visualization, A.G.; supervision, E.H.; project administration, E.H.; funding acquisition, E.H. All authors have read and agreed to the published version of the manuscript.

Funding: This research was funded by a Horizon ERC (European Union) grant (number 101045042) as part of Project CURE. The views and opinions expressed herein are solely those of the authors, and do not necessarily reflect those of the European Union or the European Research Council Executive Agency; neither the European Union nor the granting authority can be held responsible for them.

Informed Consent Statement: Specific patient consent was waived due to the retrospective study design.

Data Availability Statement: Data are contained within the article.

Conflicts of Interest: The authors declare no conflicts of interest.

Abbreviations

The following abbreviations are used in this manuscript:

IA	Intracranial Aneurysm
CFD	Computational Fluid Dynamics
CoW	Circle of Willis
WSS	Wall Shear Stress
OSI	Oscillatory Shear Index
ICA	Internal Carotid Artery
MCA	Middle Cerebral Artery
PCA	Posterior Cerebral Artery
ACA	Anterior Cerebral Artery
ACom	Anterior Communicating Artery
PCom	Posterior Communicating Artery

References

1. Wójtowicz, K.; Przepiorka, L.; Kujawski, S.; Marchel, A.; Kunert, P. Unruptured Anterior Communicating Artery Aneurysms: Management Strategy and Results of a Single-Center Experience. *J. Clin. Med.* **2023**, *12*, 4619. [CrossRef] [PubMed]
2. Juvela, S. Outcome of Patients with Multiple Intracranial Aneurysms after Subarachnoid Hemorrhage and Future Risk of Rupture of Unruptured Aneurysm. *J. Clin. Med.* **2021**, *10*, 1712. [CrossRef] [PubMed]
3. Pagiola, I.; Mihalea, C.; Caroff, J.; Ikka, L.; Chalumeau, V.; Iacobucci, M.; Ozanne, A.; Gallas, S.; Marques, M.; Nalli, D.; et al. The PHASES score: To treat or not to treat? Retrospective evaluation of the risk of rupture of intracranial aneurysms in patients with aneurysmal subarachnoid hemorrhage. *J. Neuroradiol.* **2020**, *47*, 349–352. [CrossRef]
4. Cebral, J.R.; Mut, F.; Raschi, M.; Scrivano, E.; Ceratto, R.; Lylyk, P.; Putman, C.M. Aneurysm rupture following treatment with flow-diverting stents: Computational hemodynamics analysis of treatment. *Am. J. Neuroradiol.* **2011**, *32*, 27–33. [CrossRef] [PubMed]
5. Janiga, G.; Berg, P.; Sugiyama, S.; Kono, K.; Steinman, D.A. The computational fluid dynamics rupture challenge 2013—Phase I: Prediction of rupture status in intracranial aneurysms. *Am. J. Neuroradiol.* **2015**, *36*, 530–536. [CrossRef] [PubMed]

6. Berg, P.; Roloff, C.; Beuing, O.; Voß, S.; Sugiyama, S.; Aristokleous, N.; Anayiotos, A.S.; Ashton, N.; Revell, A.; Bressloff, N.W.; et al. The Computational Fluid Dynamics Rupture Challenge 2013—Phase II: Variability of Hemodynamic Simulations in Two Intracranial Aneurysms. *J. Biomech. Eng.* **2015**, *137*, 121008. [CrossRef] [PubMed]
7. Valen-Sendstad, K.; Bergersen, A.W.; Shimogonya, Y.; Goubergrits, L.; Bruening, J.; Pallares, J.; Cito, S.; Piskin, S.; Pekkan, K.; Geers, A.J.; et al. Real-World Variability in the Prediction of Intracranial Aneurysm Wall Shear Stress: The 2015 International Aneurysm CFD Challenge. *Cardiovasc. Eng. Technol.* **2018**, *9*, 544–564. [CrossRef]
8. Berg, P.; Voß, S.; Saalfeld, S.; Janiga, G.; Bergersen, A.; Valen-Sendstad, K.; Bruening, J.; Goubergrits, L.; Spuler, A.; Cancelliere, N.; et al. Multiple Aneurysms AnaTomy CHallenge 2018 (MATCH): Phase I: Segmentation. *Cardiovasc. Eng. Technol.* **2018**, *9*, 565–581. [CrossRef]
9. Voß, S.; Beuing, O.; Janiga, G.; Berg, P. Multiple Aneurysms AnaTomy CHallenge 2018 (MATCH)-Phase Ib: Effect of morphology on hemodynamics. *PLoS ONE* **2019**, *14*, e0216813. [CrossRef]
10. Berg, P.; Voß, S.; Janiga, G.; Saalfeld, S.; Bergersen, A.W.; Valen-Sendstad, K.; Bruening, J.; Goubergrits, L.; Spuler, A.; Chiu, T.L.; et al. Multiple Aneurysms AnaTomy CHallenge 2018 (MATCH)—phase II: Rupture risk assessment. *Int. J. Comput. Assist. Radiol. Surg.* **2019**, *14*, 1795–1804. [CrossRef]
11. Berg, P.; Saalfeld, S.; Voß, S.; Beuing, O.; Janiga, G. A review on the reliability of hemodynamic modeling in intracranial aneurysms: Why computational fluid dynamics alone cannot solve the equation. *Neurosurg. Focus* **2019**, *47*, E15. [CrossRef] [PubMed]
12. Marsden, A.L.; Feinstein, J.A.; Taylor, C.A. A computational framework for derivative-free optimization of cardiovascular geometries. *Comput. Methods Appl. Mech. Eng.* **2008**, *197*, 1890–1905. [CrossRef]
13. Helthuis, J.H.; van Doormaal, T.P.; Hillen, B.; Bleys, R.L.; Harteveld, A.A.; Hendrikse, J.; van der Toorn, A.; Brozici, M.; Zwanenburg, J.J.; van der Zwan, A. Branching Pattern of the Cerebral Arterial Tree. *Anat. Rec.* **2019**, *302*, 1434–1446. [CrossRef] [PubMed]
14. Chnafa, C.; Valen-Sendstad, K.; Brina, O.; Pereira, V.M.; Steinman, D.A. Improved reduced-order modelling of cerebrovascular flow distribution by accounting for arterial bifurcation pressure drops. *J. Biomech.* **2017**, *51*, 83–88. [CrossRef] [PubMed]
15. Saalfeld, S.; Voß, S.; Beuing, O.; Preim, B.; Berg, P. Flow-splitting-based computation of outlet boundary conditions for improved cerebrovascular simulation in multiple intracranial aneurysms. *Int. J. Comput. Assist. Radiol. Surg.* **2019**, *14*, 1805–1813. [CrossRef] [PubMed]
16. Rosner, J.; Reddy, V.; Lui, F. *Neuroanatomy, Circle of Willis*, 1st ed.; StatPearls Publishing: St. Petersburg, FL, USA, 2022.
17. Devault, K.; Gremaud, P.A.; Novak, V.; Olufsen, M.S.; Vernières, G.; Peng, Z. Blood Flow in the Circle of Willis: Modelling and Calibration. *Multiscale Model. Simul.* **2008**, *7*, 888–909. [CrossRef] [PubMed]
18. Malm, J.; Birnefeld, J.; Zarrinkoob, L.; Wåhlin, A.; Eklund, A. Hemodynamic Disturbances in Posterior Circulation Stroke: 4D Flow Magnetic Resonance Imaging Added to Computed Tomography Angiography. *Front. Neurosci.* **2021**, *15*, 656769. [CrossRef]
19. Hindenes, L.B.; Håberg, A.K.; Johnsen, L.H.; Mathiesen, E.B.; Robben, D.; Vangberg, T.R. Variations in the circle of willis in a large population sample using 3D TOF angiography: The tromsø study. *PLoS ONE* **2020**, *15*, e0241373. [CrossRef]
20. Chnafa, C.; Brina, O.; Pereira, V.M.; Steinman, D.A. Better Than Nothing: A Rational Approach for Minimizing the Impact of Outflow Strategy on Cerebrovascular Simulations. *Am. J. Neuroradiol.* **2018**, *39*, 337–343. [CrossRef]
21. Castro, M.; Putman, C.; Cebral, J. Computational Fluid Dynamics Modeling of Intracranial Aneurysms: Effects of Parent Artery Segmentation on Intra-Aneurysmal Hemodynamics. *Am. J. Neuroradiol.* **2006**, *27*, 1703–1709.
22. Dennis, K.D.; Kallmes, D.F.; Dragomir-Daescu, D. Cerebral aneurysm blood flow simulations are sensitive to basic solver settings. *J. Biomech.* **2017**, *57*, 46–53. [CrossRef] [PubMed]
23. Britz, G.; Golshani, K.; Ferrell, A.; Zomorodi, A.; Smith, T. A review of the management of posterior communicating artery aneurysms in the modern era. *Surg. Neurol. Int.* **2010**, *1*, 88. [CrossRef] [PubMed]
24. Geuzaine, C.; Remacle, J.F. Gmsh: A 3-D Finite Element Mesh Generator with built-in Pre- and Post-Processing Facilities. *Int. J. Numer. Methods Eng.* **2009**, *79*, 1309–1331. [CrossRef]
25. Hachem, E.; Rivaux, B.; Kloczko, T.; Digonnet, H.; Coupez, T. Stabilized finite element method for incompressible flows with high Reynolds number. *J. Comput. Phys.* **2010**, *229*, 8643–8665. [CrossRef]
26. Coupez, T.; Hachem, E. Solution of high-Reynolds incompressible flow with stabilized finite element and adaptive anisotropic meshing. *Comput. Methods Appl. Mech. Eng.* **2013**, *267*, 65–85. [CrossRef]
27. Meliga, P.; Hachem, E. Time-accurate calculation and bifurcation analysis of the incompressible flow over a square cavity using variational multiscale modeling. *J. Comput. Phys.* **2019**, *376*, 952–972. [CrossRef]
28. Valen-Sendstad, K.; Steinman, D.A. Mind the gap: Impact of computational fluid dynamics solution strategy on prediction of intracranial aneurysm hemodynamics and rupture status indicators. *Am. J. Neuroradiol.* **2014**, *35*, 536–543. [CrossRef] [PubMed]
29. Goetz, A.; Rico, P.J.; Chau, Y.; Sédat, J.; Larcher, A.; Hachem, E. Proposal for Numerical Benchmarking of Fluid-Structure Interaction in Cerebral Aneurysms. *arXiv* **2023**, arXiv:2308.08301.
30. Hodis, S.; Uthamaraj, S.; Smith, A.L.; Dennis, K.D.; Kallmes, D.F.; Dragomir-Daescu, D. Grid convergence errors in hemodynamic solution of patient-specific cerebral aneurysms. *J. Biomech.* **2012**, *45*, 2907–2913. [CrossRef]
31. Abraham, F.; Behr, M.; Heinkenschloss, M. Shape optimization in unsteady blood flow: A numerical study of non-Newtonian effects. *Comput. Methods Biomech. Biomed. Eng.* **2005**, *8*, 201–212. [CrossRef]
32. Xiang, J.; Tremmel, M.; Kolega, J.; Levy, E.I.; Natarajan, S.K.; Meng, H. Newtonian viscosity model could overestimate wall shear stress in intracranial aneurysm domes and underestimate rupture risk. *J. Neurointerv. Surg.* **2012**, *4*, 351–357. [CrossRef] [PubMed]

33. Gambaruto, A.M.; Janela, J.; Moura, A.; Sequeira, A. Sensitivity of hemodynamics in a patient specific cerebral aneurysm to vascular geometry and blood rheology. *Math. Biosci. Eng.* **2011**, *8*, 409–423. [PubMed]
34. Tanaka, H.; Fujita, N.; Enoki, T.; Matsumoto, K.; Watanabe, Y.; Murase, K.; Nakamura, H. Relationship between Variations in the Circle of Willis and Flow Rates in Internal Carotid and Basilar Arteries Determined by Means of Magnetic Resonance Imaging with Semiautomated Lumen Segmentation: Reference Data from 125 Healthy Volunteers. *AJNR Am. J. Neuroradiol.* **2006**, *27*, 1770–1775. [PubMed]
35. Vignon-Clementel, I.E.; Alberto Figueroa, C.; Jansen, K.E.; Taylor, C.A. Outflow boundary conditions for three-dimensional finite element modeling of blood flow and pressure in arteries. *Comput. Methods Appl. Mech. Eng.* **2006**, *195*, 3776–3796. [CrossRef]
36. Janiga, G.; Berg, P.; Beuing, O.; Neugebauer, M.; Gasteiger, R.; Preim, B.; Rose, G.; Skalej, M.; Thevenin, D. Recommendations for accurate numerical blood flow simulations of stented intracranial aneurysms. *Biomed. Tech.* **2013**, *58*, 303–314. [CrossRef]
37. Boussel, L.; Rayz, V.L.; McCulloch, C.; Martin, A.; Acevedo-Bolton, G.; Lawton, M.; Higashida, R.; Smith, W.S.; Young, W.L.; Saloner, D. Aneurysm growth occurs at region of low wall shear stress: Patient-specific correlation of hemodynamics and growth in a longitudinal study. *Stroke* **2008**, *39*, 2997–3002. [CrossRef]
38. Urschel, K.; Tauchi, M.; Achenbach, S.; Dietel, B. Investigation of wall shear stress in cardiovascular research and in clinical practice—From bench to bedside. *Int. J. Mol. Sci.* **2021**, *22*, 5635. [CrossRef]
39. Cebral, J.; Detmer, F.; Chung, B.; Choque-Velasquez, J.; Rezai Jahromi, B.; Lehto, H.; Tulamo, R.; Hernesniemi, J.; Niemela, M.; Yu, A.; et al. Local Hemodynamic Conditions Associated with Focal Changes in the Intracranial Aneurysm Wall. *AJNR Am. J. Neuroradiol.* **2019**, *40*, 510–516.
40. Meng, H.; Tutino, V.M.; Xiang, J.; Siddiqui, A. High WSS or Low WSS? Complex interactions of hemodynamics with intracranial aneurysm initiation, growth, and rupture: Toward a unifying hypothesis. *Am. J. Neuroradiol.* **2014**, *35*, 1254–1262. [CrossRef]
41. Malek, A. Hemodynamic Shear Stress and Its Role in Atherosclerosis. *JAMA* **1999**, *282*, 2035. [CrossRef]
42. Furukawa, K.; Ishida, F.; Tsuji, M.; Miura, Y.; Kishimoto, T.; Shiba, M.; Tanemura, H.; Umeda, Y.; Sano, T.; Yasuda, R.; et al. Hemodynamic characteristics of hyperplastic remodeling lesions in cerebral aneurysms. *PLoS ONE* **2018**, *13*, e0191287. [CrossRef] [PubMed]
43. Mazzi, V.; Gallo, D.; Calò, K.; Najafi, M.; Khan, M.O.; De Nisco, G.; Steinman, D.A.; Morbiducci, U. A Eulerian method to analyze wall shear stress fixed points and manifolds in cardiovascular flows. *Biomech. Model. Mechanobiol.* **2020**, *19*, 1403–1423. [CrossRef] [PubMed]
44. Sheikh, M.A.A.; Shuib, A.S.; Mohyi, M.H.H. A review of hemodynamic parameters in cerebral aneurysm. *Interdiscip. Neurosurg. Adv. Tech. Case Manag.* **2020**, *22*, 100716. [CrossRef]
45. Jongen, J.C.; Franke, C.L.; Ramos, L.M.; Wilmink, J.T.; Van Gijn, J. Direction of Flow in Posterior Communicating Artery on Magnetic Resonance Angiography in Patients with Occipital Lobe Infarcts. *Stroke* **2004**, *35*, 104–108. [CrossRef] [PubMed]
46. Zarrinkoob, L.; Ambarki, K.; Wåhlin, A.; Birgander, R.; Eklund, A.; Malm, J. Blood flow distribution in cerebral arteries. *J. Cereb. Blood Flow Metab.* **2015**, *35*, 648–654. [CrossRef]
47. Mynard, J.P.; Valen-Sendstad, K. A unified method for estimating pressure losses at vascular. *Int. J. Numer. Methods Biomed. Eng.* **2015**, *31*. [CrossRef]
48. Hacein-Bey, L.; Provenzale, J.M. Current Imaging Assessment and Treatment of Intracranial Aneurysms. *Am. J. Roentgenol.* **2011**, *196*, 32–44. [CrossRef]
49. Chen, J.; Li, M.; Zhu, X.; Chen, Y.; Zhang, C.; Shi, W.; Chen, Q.; Wang, Y. Anterior Communicating Artery Aneurysms: Anatomical Considerations and Microsurgical Strategies. *Front. Neurol.* **2020**, *11*, 1020. [CrossRef]
50. Zhang, H.; Fujiwara, N.; Kobayashi, M.; Yamada, S.; Liang, F.; Takagi, S.; Oshima, M. Development of a Numerical Method for Patient-Specific Cerebral Circulation Using 1D–0D Simulation of the Entire Cardiovascular System with SPECT Data. *Ann. Biomed. Eng.* **2016**, *44*, 2351–2363. [CrossRef]
51. Hindenes, L.B.; Ingebrigtsen, T.; Isaksen, J.G.; Håberg, A.K.; Johnsen, L.H.; Herder, M.; Mathiesen, E.B.; Vangberg, T.R. Anatomical variations in the circle of Willis are associated with increased odds of intracranial aneurysms: The Tromsø study. *J. Neurol. Sci.* **2023**, *452*, 120740. [CrossRef]
52. Feng, L.; Mao, H.J.; Zhang, D.D.; Zhu, Y.C.; Han, F. Anatomical variations in the Circle of Willis and the formation and rupture of intracranial aneurysms: A systematic review and meta-analysis. *Front. Neurol.* **2023**, *13*, 1098950. [CrossRef] [PubMed]